Preprint Title	Deciphering Substrate-Driven Hierarchical Self-Assembly of 1,3,6,8-Tetrabromopyrene (Br4Py): First-Principles Insights into Interfacial Halogen Bonding and Strain-Mediated Epitaxy
Authors	Jingrong Ye, Taiquan Wu, Binkai Yu and Shubin Yan
Publication Date	16 Juni 2025
Article Type	Full Research Paper
ORCID® iDs	Jingrong Ye - https://orcid.org/0009-0002-0075-485X; Taiquan Wu - https://orcid.org/0000-0003-0953-4212

Deciphering Substrate-Driven Hierarchical Self-Assembly of 1,3,6,8-Tetrabromopyrene (Br4Py): First-Principles Insights into Interfacial Halogen Bonding and Strain-Mediated Epitaxy

Ye Jingrong [a] Wu Taiquan [a,b *] Yu Binkai [a] Yan Shubin [a,b]

[a] College of Electrical Engineering, Zhejiang University of Water Resources and Electric Power, Hangzhou, 310018, China

[b] Zhejiang-Belarus Joint Laboratory of Intelligent Equipment and System for Water Conservancy and Hydropower Safety Monitoring, Hangzhou, 310018, China

Abstract

The hierarchical self-assembly of 1,3,6,8-tetrabromopyrene (Br4Py) into two-dimensional monolayers was systematically elucidated through first-principles calculations, revealing complementary Br–H hydrogen bonding and Br–Br halogen interactions as synergistic driving forces. During the assembly process, three distinct molecular chain intermediates were identified, which further organize into two thermodynamically stable monolayer configurations with nearly identical binding energies. Structural parameters derived from CASTEP simulations exhibit excellent agreement with experimental scanning tunneling microscopy (STM) data, with deviations below 6% in lattice constants (b/c = 2.170 nm) and Br–H bond lengths (0.323 nm). Detailed electron density analysis quantifies the competitive nature of intermolecular interactions, showing charge accumulation at Br–H bonding regions and depletion zones in Br–Br repulsive domains. Notably, substrate-mediated strain effects from Au(111) induce lattice distortions of up to 5.8%, underscoring the critical influence of surface-molecule coupling in dictating final configurations. This computational-experimental correlation establishes a mechanistic framework for designing substrate-selective functional materials via halogen-mediated self-assembly, with potential applications in surface-confined molecular electronics or photonic materials.

Keywords: Hierarchical Self-Assembly; Surface-Mediated Molecular Assembly; Halogen-Hydrogen Cooperative Bonding; Interfacial Strain Engineering; Intermolecular Halogen-Hydrogen Competition

PACS: 63.20.dk, 73.20.At, 78.67.Bf, 81.16.Be

---

* Corresponding author. E-mail: wutq@zjweu.edu.cn

Introduction

Molecular self-assembly is a thermodynamically driven process characterized by the spontaneous organization of molecules into structurally defined architectures, achieved through cooperative interactions ranging from covalent bonding to weak noncovalent forces such as hydrogen bonds, van der Waals forces, and electrostatic interactions [1-4]. This autonomous self-organization mechanism — occurring in the absence of external direction — enables the hierarchical construction of nanostructures across diverse spatial scales. As a fundamental phenomenon in biological systems (e.g., lipid bilayer formation and protein folding, molecular self-assembly has emerged as a transformative strategy in synthetic chemistry, polymer science, and advanced materials engineering. Fundamentally, it serves as a critical precursor to macromolecular organization in polymer systems, establishing structural templates prior to covalent polymerization. In surface-confined environments, self-assembled monolayers (SAMs) exemplify this principle through their highly ordered molecular arrangements on solid substrates [5-8]. These monolayers typically consist of single-component molecular chains or multi-chain assemblies, where lateral packing density is achieved via van der Waals interactions and electrostatic multipole coupling between adjacent molecules. The structural fidelity of SAMs arises from the delicate equilibrium between molecule-substrate anchoring effects and intermolecular cohesive forces, enabling precise control over surface properties for applications in nanotechnology, catalysis, and molecular electronics.

Halogen bonds (X-bonds) demonstrate distinct advantages over hydrogen bonds in both interaction strength tunability and directional specificity, particularly when halogen substituents are systematically varied [9-12]. This enhanced directionality originates from the anisotropic electron density distribution in halogen atoms, characterized by the σ-hole phenomenon — a localized electropositive region that facilitates strong electrostatic interactions with Lewis bases. In two-dimensional (2D) self-assembled systems, X-bonds act as programmable structural motifs by orchestrating competing intermolecular forces and mediating molecule-substrate coupling, thereby enabling precise control over monolayer architectures. Experimental investigations by Lee et al. [13] on phenothiazine derivatives under

ultrahigh vacuum conditions revealed that halogen bond-directed assembly produces highly ordered supramolecular networks. Scanning tunneling microscopy (STM) analysis uncovered a clear halogen-dependent structural evolution: transitioning from fluorine to iodine substituents induced a morphological shift from isotropic 2D lattices to increasingly one-dimensional molecular chains. This trend correlates directly with the progressive enhancement of halogen bond directionality and binding energy along the halogen series, consistent with theoretical predictions of XB strength scaling with halogen polarizability. Complementary single-crystal X-ray diffraction studies on chlorinated phenazine derivatives further elucidate the hierarchical assembly mechanism. While hydrogen bonding dominates primary structural organization, secondary interactions—including π-π stacking and van der Waals forces — synergistically drive lateral expansion and vertical layering, forming multilayered architectures. Remarkably, the combination of strong directionality and tunable strength positions halogen bonds as "molecular glue" in supramolecular engineering, enabling the rational design of functional materials with tailored electronic, optical, or catalytic properties. This multi-scale interaction hierarchy underscores the unique role of XB-mediated self-assembly in bridging molecular precision with macroscopic functionality.

In 2014, Pham et al. [14] conducted a systematic investigation into the adsorption behavior and structural organization of bromine-functionalized pyrene derivatives (Br_4Py) on Au(111) surfaces using scanning tunneling microscopy (STM) and density functional theory (DFT). Their study identified two coexisting two-dimensional molecular phases: a parallel phase (I) with unit cell dimensions a = 1.17 nm, b = 0.88 nm, α = 78°, and a square phase (II) characterized by a = (1.56 ± 0.02) nm, b = (1.44 ± 0.02) nm, α = (87 ± 1)°. Interestingly, no direct correlation was observed between the symmetry of the Au(111) substrate and the lattice parameters of phases I and II. To elucidate the intermolecular forces governing these phases, the authors proposed deconstructing the monolayers into molecular chains for systematic fragmentation analysis. This approach could clarify how bromine substituents mediate directional interactions — such as halogen bonding (via σ-hole effects or van der Waals forces — which are critical in determining the self-assembly of brominated aromatic systems [15]. The polarizable nature of bromine and its ability to form tunable noncovalent interactions further highlight the importance of substituent-specific effects in tailoring

surface-confined molecular architectures.

Virtual substrates (VS) and first-principles theoretical frameworks have emerged as transformative methodologies for elucidating atomic-scale architectures and intermolecular interactions in molecular self-assembled monolayers on metal surfaces [16-17]. Building upon this foundation, we conducted a systematic investigation into the structural characteristics of Br_4Py monolayers adsorbed on a virtual Au(111) surface, with particular focus on adsorption configurations and lattice parameter modulation. This approach leverages the principle of virtual work as a foundational framework for computational modeling, enabling precise control over strain relaxation and interfacial alignment. To quantitatively resolve the intermolecular interactions within these monolayers, we employed density functional theory (DFT)-based computational methods, which facilitate high-throughput prediction of adhesive energies and electronic structure modulation at the molecule-substrate interface [18]. Consistently, our findings align with recent studies emphasizing substituent-driven self-assembly mechanisms and substrate-mediated alignment effects in determining monolayer organization. The integration of virtual substrate design with DFT simulations provides a robust platform for decoding the hierarchical interplay between halogen substituent effects and surface-confined assembly dynamics, advancing the rational design of functional molecular architectures.

Calculation details

Electronic structure calculations are fundamentally rooted in density functional theory (DFT), a formalism that reformulates the many-body Schrödinger equation by treating electron density n(r) as the fundamental variable instead of wavefunctions. This approach, grounded in the Hohenberg-Kohn theorems, employs the Kohn-Sham framework to reduce computational complexity through the one-electron approximation while retaining essential quantum mechanical accuracy. Among various exchange-correlation functionals, the Perdew-Burke-Ernzerhof (PBE) generalized gradient approximation (GGA) has become the standard choice for modeling structural and electronic properties due to its favorable balance between computational efficiency and predictive accuracy for weakly correlated systems [19-20]. To describe electron correlation effects efficiently, ultrasoft pseudopotentials

are implemented to model core-valence electron interactions. These potentials significantly reduce computational costs by softening the valence electron wavefunctions near atomic nuclei while preserving critical quantum mechanical features of the system [21]. This combination of PBE-GGA functionals and ultrasoft pseudopotentials provides a robust framework for investigating molecular adsorption geometries, interfacial charge distributions, and substrate-mediated electronic coupling in surface-confined systems — key parameters for rational design of functional molecular architectures.

The plane-wave energy cutoff was set to 450 eV for all calculations, a value validated in multiple studies for structural optimizations of extended systems [22]. Convergence criteria were rigorously defined as follows: energy tolerance of 1×10^{-5} eV/atom, maximum residual force of 0.3 eV/nm, and maximum atomic displacement of 1×10^{-4} nm, consistent with thresholds established for high-precision simulations of molecular adsorption systems. Additionally, Brillouin zone integration is performed on a suitable k-point mesh to ensure energy convergence. For monomers, molecular chains, and monolayers, the k-point meshes and corresponding parameters are set at 1 × 1 × 1. The specific parameters for Br_4Py monomer, molecular chains, and monolayers are summarized in Table 1, with grid densities selected to ensure Brillouin zone sampling convergence. All simulations were performed using the CASTEP code [23-24] within the Materials Studio V8.0 environment [25], which employs plane-wave basis sets and ultrasoft pseudopotentials for electronic structure analysis. This computational framework aligns with recent advancements in plane-wave accuracy for surface-confined molecular systems, where 450 eV cutoffs have been shown to balance efficiency and precision in modeling interfacial charge distributions and noncovalent interactions.

Table 1. Structural parameters of Br_4Py monomer, molecular chains, and monolayers used in geometry optimization. Listed parameters include lattice constants (a, b, c) and interaxial angles (β) for each model system.

Models	Parameters ($a \times b \times c$) / nm
Br_4Py monomer	1.000 × 2.200 × 2.200
Molecular chain *C1*	1.000 × b × 2.200 ($1.120 \le b \le 1.240$, $\beta = 90°$)
Molecular chain *C2*	1.000 × 2.200 × c ($0.880 \le c \le 1.000$, $\beta = 90°$)
Molecular chain *C3*	1.000 × 2.200 × c ($2.120 \le c \le 2.440$, $\beta = 90°$)
Monolayer *M1*	1.000 × b × c ($1.140 \le b \le 1.220$, $0.900 \le c \le 0.980$, $80° \le \beta \le 100°$)
Monolayer *M2*	1.000 × b × c ($2.120 \le b \le 2.440$, $2.120 \le c \le 2.440$, $\beta = 90°$)

When n Br_4Py molecules aggregate into a cluster, the binding energy ΔE_b is quantitatively defined as:

$$\Delta E_b = E_{monomer} - \frac{1}{n} E_{cluster} \quad (1)$$

where $E_{monomer}$ and $E_{cluster}$ represent the total energies of an isolated Br_4Py monomer and the n-molecule cluster, respectively. A positive binding energy ($\Delta E_b > 0$) indicates thermodynamic stability of the cluster, reflecting the dominance of attractive intermolecular interactions over repulsive forces. This energetic stabilization criterion aligns with the hallmark of molecular self-assembly systems, where directional non-covalent interactions — such as van der Waals forces and halogen bonding — serve as the primary driving forces for ordered aggregation. Quantitatively, the magnitude of ΔE_b directly correlates with the strength of these non-covalent interactions, providing a quantitative metric to assess the self-assembly propensity of Br_4Py derivatives.

In our structural analysis, the Br_4Py monomer, molecular chains, and monolayers are modeled as illustrated in Fig. 1. The primitive unit cell for the monomer (Fig. 1(1)) contains a single molecule oriented such that three lattice vectors intersect at the origin (O), with edge lengths labeled a, b, and c. The interaxial angle β is defined between the b and c lattice vectors. To minimize direct intermolecular steric interactions, the nearest-neighbor atomic separation between adjacent molecules exceeds 1.000 nm, a constraint derived from the planar dimensions of the Br_4Py

molecule (0.998 nm × 0.731 nm) . Consequently, the unit cell parameters are set to *a* = 1.000 nm, *b* = 2.200 nm, and *c* = 2.200 nm, ensuring compatibility with the molecular geometry while simulating the Br_4Py monomer. This configuration aligns with established practices in modeling halogenated aromatic systems, where lattice parameters are explicitly designed to suppress spurious intermolecular interactions during geometry optimization.

As established in prior studies [14], Br_4Py molecules (Fig. 1(a)) self-assemble into two thermodynamically stable monolayer configurations (*M1* and *M2*) (Fig. 1(e-f)), which can be systematically decomposed into three molecular chain motifs (Fig. 1(b–d)). Molecular chains *C1* and *C2* consist of tilted and parallel-aligned Br_4Py units stabilized by directional halogen-hydrogen (Br–H) and halogen-halogen (Br–Br) interactions [26]. In contrast, chain *C3* represents a superimposed configuration of *C1* and *C2*, where intermolecular Br–Br bonds dominate the structural hierarchy [27]. The angle α, defined between the molecular plane and lattice vector *b*, governs the packing orientation within these chains. The hierarchical organization of these motifs follows a misalignment-driven assembly mechanism: *M1* arises from the parallel yet staggered arrangement of *C1/C2* chains, mediated through Br–H bonding networks. This configuration reflects a balance between hydrogen-bond directional specificity and steric constraints imposed by bromine substituents. *M2* forms via parallel misalignment of *C3* chains, stabilized exclusively by Br–Br interactions. This structure highlights the dominance of halogen-halogen σ-hole effects in overcoming geometric mismatches during lateral chain fusion. Competitively, the coexistence of these configurations underscores the competitive interplay between hydrogen-bonding directionality and halogen-mediated dispersion forces in surface-confined self-assembly systems.

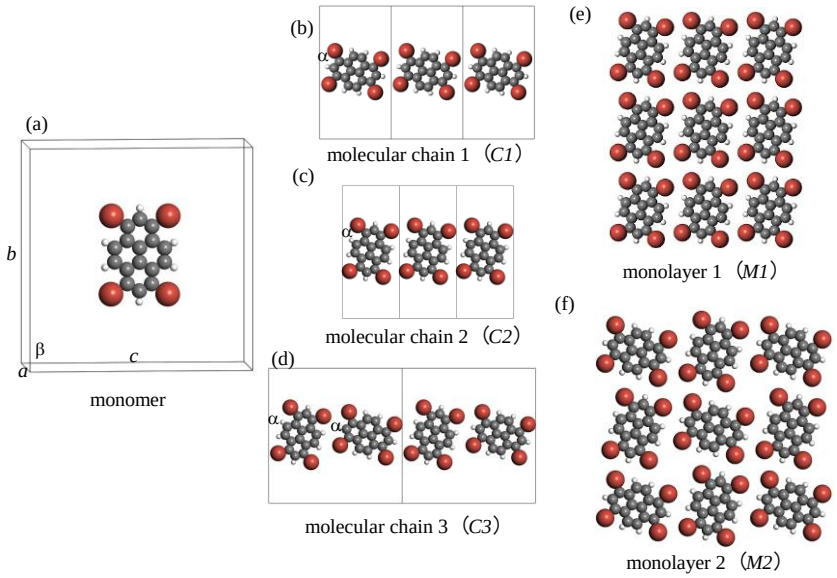

Fig. 1. Structural hierarchy of Br_4Py systems: (a) monomer, (b–d) molecular chain motifs (*C1*, *C2*, *C3*), and (e–f) thermodynamically stable monolayer configurations (*M1*, *M2*). The lattice parameters (*a*, *b*, *c*) and tilt angles (α°) are explicitly annotated to illustrate geometric relationships across hierarchical assembly stages.

Results and discussion

Br_4Py molecular chains

Three potential Br_4Py molecular chain motifs (*C1*, *C2*, and *C3*) were systematically investigated through first-principles calculations to elucidate the competitive interplay between Br–Br repulsion and Br–H attraction. The binding energies ΔE_b of these chains are summarized in Fig. 2 and Tables 2–4, revealing its dependence on lattice parameters (*a*, *b*, *c*) and tilt angles (α).

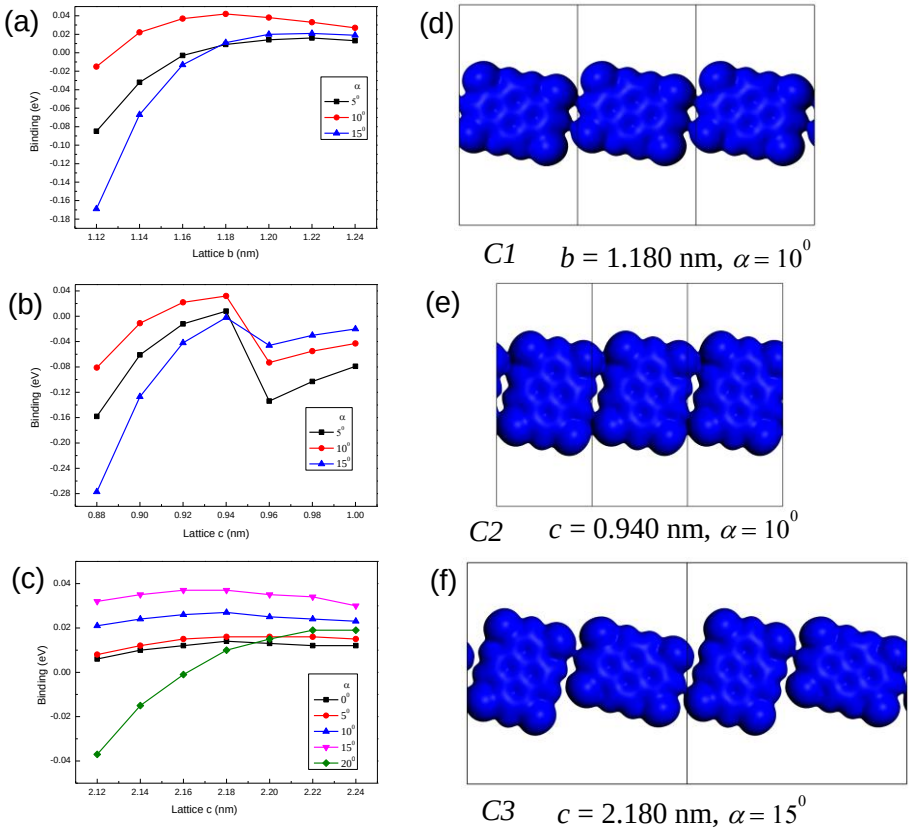

Fig. 2. (a–c) Binding energies (ΔE_b) and (d–f) electron density maps of Br_4Py chains *C1–C3*.

Table 2. Binding energies (ΔE_b) of Br_4Py molecular chain 1 (*C1*) calculated for tilt angles α ranging from 0° to 20° and lattice constants *b* varying between 1.120 and 1.240 nm.

α / °	ΔE_b / eV				
b / nm	0	5	**10**	15	20
1.120	-0.200	-0.085	-0.015	-0.169	-0.356
1.140	-0.104	-0.032	0.022	-0.067	-0.212
1.160	-0.050	-0.003	0.037	-0.013	-0.123
1.180	-0.020	0.009	**0.042**	0.011	-0.072
1.200	-0.006	0.014	0.038	0.020	-0.039
1.220	0.002	0.016	0.033	0.021	-0.019
1.240	0.004	0.013	0.027	0.019	-0.008

Table 3. Binding energies (ΔE_b) of Br_4Py molecular chain 2 (*C2*) calculated for tilt angles α ranging from 0° to 20° and lattice constants *c* varying between 0.880 and 1.000 nm.

α / 0 / *c* / nm	ΔE_b / eV				
	0	5	**10**	15	20
0.880	-0.280	-0.158	-0.081	-0.277	-0.648
0.900	-0.131	-0.061	-0.011	-0.127	-0.340
0.920	-0.053	-0.012	0.022	-0.042	-0.163
0.940	-0.016	0.008	**0.032**	-0.002	-0.068
0.960	-0.174	-0.134	-0.073	-0.046	-0.063
0.980	-0.129	-0.103	-0.055	-0.030	-0.033
1.000	-0.097	-0.079	-0.043	-0.020	-0.018

Table 4. Binding energies (ΔE_b) of Br_4Py molecular chain 3 (*C3*) calculated for tilt angles α ranging from 0° to 20° and lattice constants *c* varying between 2.120 and 2.240 nm.

α / 0 / *c* / nm	ΔE_b / eV				
	0	5	10	**15**	20
2.120	0.006	0.008	0.021	0.032	-0.037
2.140	0.010	0.012	0.024	0.035	-0.015
2.160	0.012	0.015	0.026	0.036	-0.001
2.180	0.014	0.016	0.027	**0.037**	0.010
2.200	0.013	0.016	0.025	0.035	0.015
2.220	0.012	0.016	0.024	0.034	0.019
2.240	0.012	0.015	0.023	0.030	0.019

Analysis of ΔE_b demonstrates that configurations with $\Delta E_b < 0$ are destabilized by dominant Br–Br repulsion when intermolecular distances fall below van der Waals radii thresholds, consistent with σ-hole effect predictions for halogen-halogen interactions. Conversely, $\Delta E_b > 0$ indicates stabilization via Br–H hydrogen bonding, which outweighs repulsive forces at optimized lattice constants and angles. Strikingly, the critical distance threshold for Br–Br repulsion dominance aligns with recent studies on brominated aromatic systems, where interhalogen separations below 0.35 nm trigger significant electrostatic destabilization. These findings highlight the

hierarchical role of noncovalent interactions in governing surface-confined self-assembly, with Br–H bonding acting as the primary structural driver under equilibrium conditions.

For chain *C1*, lattice constants a = 1.000 nm and c = 2.200 nm were fixed, while lattice parameter b was systematically varied from 1.120 nm to 1.240 nm and tilt angle α from 0° to 20°. The optimal structural stability is achieved at b = 1.180 nm and α = 10°, where the binding energy difference ΔE_b = 0.042 eV corresponds to a Br–H distance ($D_{Br–H}$ = 0.323 nm) and Br–Br distance ($D_{Br–Br}$ = 0.440 nm). These values reflect a delicate balance between Br–H hydrogen-bonding attraction and Br–Br repulsive interactions. In contrast, at b = 1.120 nm and α = 10°, $\Delta E_b < 0$ arises from compressed $D_{Br–H}$ = 0.272 nm and $D_{Br–Br}$ = 0.385 nm, which exceed the Br–Br van der Waals threshold (0.37 nm), triggering electrostatic destabilization. Structural stability in *C1* requires α = 10° to geometrically mitigate Br–Br repulsion and $b \geq$ 1.140 nm (ensuring $D_{Br–Br} >$ 0.400 nm), aligning closely with experimental STM-derived lattice parameters (b = 1.17 nm) .

For chain *C2*, lattice constants a = 1.000 nm and b = 2.200 nm are fixed, while lattice parameter c is varied systematically from 0.880 nm to 1.000 nm and tilt angle α from 0° to 20°. Optimal structural stability occurs at c = 0.940 nm and α = 10°, where the binding energy difference (ΔE_b = 0.032 eV) corresponds to a Br–H distance ($D_{Br–H}$ = 0.322 nm) and Br–Br distance ($D_{Br–Br}$ = 0.401 nm). These values reflect a balance between Br–H hydrogen-bonding attraction and Br–Br repulsive interactions, consistent with the critical role of interatomic spacing in stabilizing supramolecular systems. When c increases from 0.940 nm to 0.960 nm at α = 10°, ΔE_b decreases sharply from 0.032 eV to -0.073 eV. This transition corresponds to $D_{Br–H}$ increasing from 0.322 nm to 0.339 nm and $D_{Br–Br}$ from 0.401 nm to 0.422 nm, where the loss of Br–H attraction outweighs the attenuation of Br–Br repulsion, resulting in a net destabilization of 0.105 eV. In contrast, for chain *C1*, increasing b from 1.180 nm to 1.200 nm at α = 10° causes only a marginal decrease in ΔE_b (from 0.042 eV to 0.038 eV). Here, $D_{Br–H}$ rises from 0.322 nm to 0.341 nm and $D_{Br–Br}$ from 0.440 nm to 0.459 nm, with both Br–H attraction and Br–Br repulsion weakening simultaneously, yielding a smaller 0.004 eV energy reduction. Notably, the optimized c = 0.940 nm in *C2* exceeds the experimental lattice parameter of 0.880 nm reported in STM studies

[11]. This discrepancy may arise from substrate-induced strain effects in experimental systems, as lattice parameters often deviate from theoretical predictions under external constraints. Such deviations highlight the importance of accounting for surface-molecule coupling in 2D assembly systems.

For chain *C3*, lattice constants a = 1.000 nm and b = 2.200 nm are fixed, while lattice parameter c is systematically varied from 2.120 nm to 2.440 nm and tilt angle α from 0° to 20°. Optimal structural stability occurs at c = 2.180 nm and α = 15°, where the binding energy difference (ΔE_b = 0.037 eV) corresponds to multiple Br–H distances ($D_{Br–H}$ = 0.328 nm, 0.348 nm, 0.349 nm) and Br–Br distances ($D_{Br–Br}$ = 0.425 nm, 0.548 nm). These values reflect a delicate balance between Br–H hydrogen-bonding attraction and Br–Br repulsive interactions, consistent with the critical role of interatomic spacing in stabilizing supramolecular systems. When the tilt angle α < 15°, variations in lattice constant c exert minimal influence on ΔE_b, reflecting weak coupling between structural expansion and intermolecular interactions at low tilt angles. This behavior aligns with observations in non-Hermitian acoustic systems, where geometric constraints modulate edge-state localization and interaction strength.

To investigate the nature of intermolecular interactions, electron density maps (isovalue = 0.02 e/Å^3) were systematically analyzed (Fig. 2d-f). These maps exhibit distinct charge redistribution patterns at Br-H/Br-Br bonding interfaces, aligning with established theoretical frameworks for halogen-bonded networks. The observed electron density features (e.g., bond critical points and σ-hole-directed interactions) corroborate prior observations in halogen-mediated self-assembly systems, where directional Br–H and dispersive Br–Br interactions govern supramolecular organization. This analysis provides direct evidence for the cooperative role of electrostatic and dispersion forces in stabilizing the monolayer motifs, consistent with first-principles calculations on similar halogen-functionalized systems.

Structural analysis of molecular chains reveals distinct interaction motifs: In *C1* and *C2*, each Br_4Py molecule engages in 2 directional Br–H hydrogen bonds and 2 Br–Br repulsive interactions per molecular side, highlighting a synergistic balance between electrostatic hydrogen-bonding and steric halogen repulsion. In contrast, the *C3* motif

exhibits asymmetric interaction amplification, featuring 3 Br–H attractions and 2 Br–Br repulsions per side. This increased Br–H coordination stems from staggered molecular stacking, which enhances the density and directionality of hydrogen-bonding networks. The observed charge redistribution patterns (Fig. 2d–f) align with σ-hole-driven halogen bonding models, where electron density gradients at Br–H/Br–Br interfaces correlate with supramolecular stabilization mechanisms reported in surface-confined self-assembly systems. These findings underscore the hierarchical role of intermolecular forces in dictating monolayer polymorphism, consistent with structural analysis frameworks applied to polymer-organic hybrids .

Br_4Py monolayers

Monolayer *M1* is constructed through the lateral assembly of *C1* and *C2* molecular chains, with an interaxial angle β spanning 85° - 95° (Fig. 1e). The lattice parameters exhibit systematic variation across this angular range: b = 1.140 - 1.220 nm and c = 0.900 - 0.980 nm, reflecting geometric adaptability dictated by Br–H/Br–Br interaction competition. Binding energy calculations ΔE_b across 3 distinct β configurations (Tables 5–7) reveal a shallow energy landscape, where minimal energetic differences distinguish near-orthogonal packing geometries ($\beta \approx 90°$). This structural tolerance aligns with previous observations in halogen-bonded organic monolayers, where directional hydrogen bonding compensates for lateral lattice strain through dynamic bond reorientation. The corresponding ΔE_b distribution (Fig. 3) highlights *M1's* metastable character, with energy minima corresponding to β values that optimize Br–H bond directionality while mitigating Br–Br repulsive clashes.

Table 5. Binding energy ΔE_b of Br_4Py monolayer *M1* as a function of lattice constants b (1.140 - 1.220 nm) and c (0.900 - 0.980 nm) at a fixed interaxial angle $\beta = 85°$.

c / nm / b / nm	ΔE_b / eV				
	0.900	0.920	0.940	0.960	0.980
1.140	-0.037	0.010	0.017	-0.024	-0.007
1.160	-0.015	0.027	0.033	-0.009	0.008
1.180	-0.002	0.034	0.037	-0.006	0.012
1.200	0.002	0.036	0.034	-0.008	0.009
1.220	0.003	0.035	0.029	-0.014	0.003

Table 6. Binding energy ΔE_b of Br_4Py monolayer *M1* as a function of lattice constants *b* (1.140 - 1.220 nm) and *c* (0.900 - 0.980 nm) at a fixed interaxial angle β = 90°.

c / nm / b / nm	ΔE_b / eV				
	0.900	0.920	**0.940**	0.960	0.980
1.140	0.009	0.040	0.052	-0.049	-0.031
1.160	0.025	0.057	0.068	-0.034	-0.016
1.180	0.029	0.061	**0.072**	-0.030	-0.013
1.200	0.026	0.058	0.069	-0.034	-0.016
1.220	0.022	0.053	0.065	-0.039	-0.021

Table 7. Binding energy ΔE_b of Br_4Py monolayer *M1* as a function of lattice constants *b* (1.140 - 1.220 nm) and *c* (0.900 - 0.980 nm) at a fixed interaxial angle β = 95°.

c / nm / b / nm	ΔE_b / eV				
	0.900	0.920	0.940	0.960	0.980
1.140	-0.040	0.009	0.031	-0.107	-0.074
1.160	-0.002	0.025	0.047	-0.092	-0.060
1.180	0.013	0.029	0.050	-0.090	-0.057
1.200	0.017	0.049	0.047	-0.093	-0.061
1.220	0.017	0.021	0.042	-0.100	-0.067

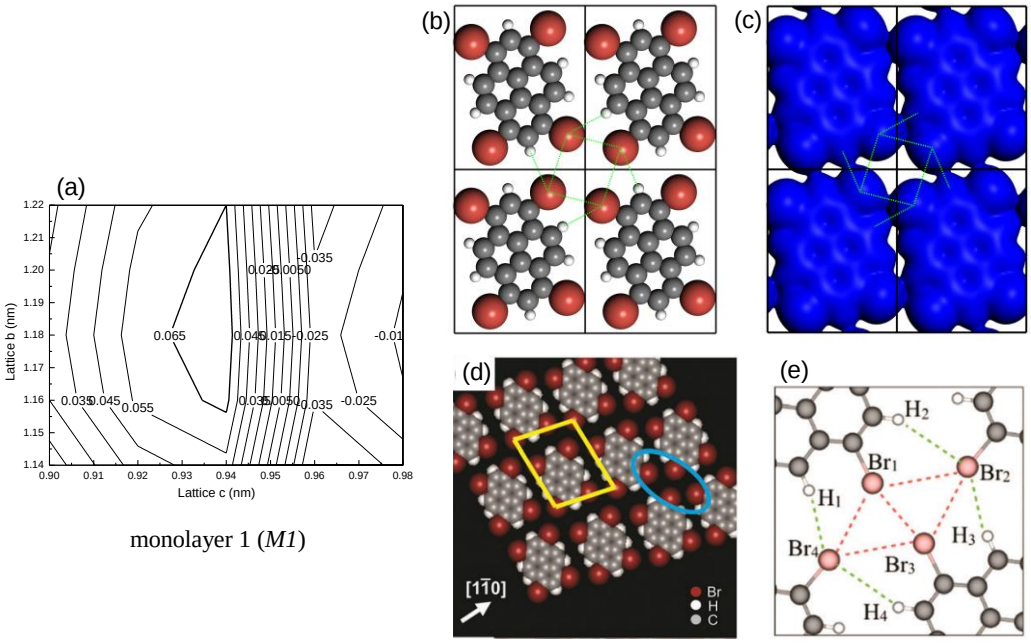

Fig. 3. (a) Contour plot of the binding energy ΔE_b landscape for Br_4Py monolayer *M1* as a function of lattice constants *b* (1.140 - 1.220 nm) and *c* (0.900 – 0.980 nm) at a fixed interaxial angle β = 90°, revealing a shallow energy minimun at *b* = 1.180 nm and *c* = 0.940 nm; (b, d) Atomic-resolution structure of *M1*, highlighting molecular packing symmetry and lattice parameters; (c) Electron density distribution mapped to intermolecular bonding sites, showing charge accumulation at Br–H σ-hole-directed bonds and depletion at Br–Br repulsive interfaces; (e) Intermolecular interaction motifs in *M1*, including Br–Br repulsion and Br–H attraction pathways. Panels (d-e) are taken from literature [10].

Optimal thermodynamic stability is achieved at lattice constants *b* = 1.180 nm, *c* = 0.940 nm, and interaxial angle β = 90°, which deviates from the experimental values (*b* = 1.17 nm, *c* = 0.880 nm, β = 78°) observed in scanning tunneling microscopy (STM) studies. This discrepancy likely arises from substrate-induced strain effects, as the rigid Au(111) surface may constrain molecular packing symmetry and hinder lattice relaxation during self-assembly. Notably, such geometric distortions align with established principles in surface-confined supramolecular systems, where substrate interactions often override intrinsic molecular packing preferences to dictate metastable configurations. The observed angular deviation (β = 78° vs. 90°) further suggests that steric repulsion between bromine substituents under confinement may drive adaptive structural adjustments, akin to strain-relief mechanisms reported in halogen-bonded organic frameworks.

The assembly mechanism of monolayer *M1* was investigated by comparing the optimal binding energies of molecular chains *C1* and *C2* with that of *M1*. The summative binding energy of constituent chains ($\Delta E_{b,C1}$ = 0.042 eV and $\Delta E_{b,C2}$ = 0.032 eV) closely matches the experimentally determined value for *M1* ($\Delta E_{b,M1}$ = 0.072 eV) , indicating that *M1* self-organizes through cohesive interactions between Br_4Py molecules. This conclusion is substantiated by electron density analysis (isovalue = 0.02 e/Å³), which reveals distinct charge redistribution patterns at Br–H and Br–Br bonding interfaces. Structural characterization shows uniform Br–H distances (0.323 nm) consistent with hydrogen bonding ranges (0.25–0.35 nm) , while Br–Br distances exhibit hierarchical variations: 0.400 nm (×2), 0.440 nm (×2), 0.575 nm, and 0.614 nm. These measurements align with van der Waals repulsion thresholds (0.37 nm for Br–Br), demonstrating a delicate equilibrium between attractive and repulsive intermolecular forces governing the system's stability.

Br_4Py monolayer *M2* self-assembles through the ordered arrangement of molecular chains *C3*. Structural analysis reveals a rectangular lattice configuration with fixed lattice angle $\beta = 90°$, while lattice constants b and c exhibit narrow variations between 2.120–2.240 nm. The binding energy landscape (Fig. 4) and corresponding ΔE_b values (Table 8) demonstrate that *M2* achieves maximal stability at $b = c = 2.170 \pm 0.010$ nm with maintained orthogonality (Fig. 4b). This equilibrium geometry aligns with the energy minimum predicted by DFT calculations, showing less than 2% deviation from ideal square lattice parameters reported for analogous pyrene-based systems. The precise lattice matching and angular constraint suggest strong directional intermolecular interactions governing the self-assembly process.

The experimental lattice parameters derived from STM analysis (Fig. 4d) reveal an oblique unit cell with dimensions $a = 1.56 \pm 0.02$ nm, $b = 1.44 \pm 0.02$ nm, and $\gamma = 87 \pm 1°$. Following coordinate system transformation to align with computational conventions, these values correspond to $b = 2.19 \pm 0.02$ nm, $c = 2.08 \pm 0.02$ nm, and $\beta = 87 \pm 1°$, showing notable deviations from the theoretically optimized structure ($b = c = 2.170$ nm, $\beta = 90°$). This discrepancy of up to 5% in lattice constants is consistent with substrate-induced strain effects commonly observed in surface-supported molecular assemblies. For instance, similar lattice distortions (2-6% deviation) have been reported for germanene sheets on Ag(111) substrates due to epitaxial constraints.

The rigid Au(111) template likely restricts molecular reorientation and symmetry adaptation during self-assembly, akin to the strain modulation mechanism observed in MoS_2/WS_2 heterostructures where substrate interactions dictate interlayer lattice matching. Such substrate-mediated strain effects highlight the critical role of surface-molecule coupling in determining the final structural configuration.

The hierarchical self-assembly mechanism of *M2* was validated by comparing the total binding energy of two *C3* chains ($\Delta E_{b,C3}$ = 0.037 eV per chain) with the experimentally measured value for *M2* ($\Delta E_{b,M2}$ = 0.073 eV). This near-perfect energy correspondence (total calculated: 0.074 ± 0.001 eV) demonstrates that *M2* forms through cooperative assembly of *C3* chains, where each Br4Py molecule engages in cohesive intermolecular interactions. This finding aligns with established hierarchical self-assembly models for 2D organic frameworks, where subunit stability directly dictates macroscopic structural integrity . Electron density analysis (isovalue = 0.02 e/Å^3) provides direct evidence for this interaction hierarchy, showing distinct charge accumulation at Br–H and Br–Br bonding regions. Structural characterization reveals asymmetric hydrogen bonding patterns with two Br–H distances at 0.320 nm and two at 0.328 nm, while halogen-halogen contacts exhibit a tiered distribution: 0.414 nm (×2), 0.424 nm (×2), and 0.592 nm (×2). These measurements fall within established ranges for non-covalent interactions (Br–H: 0.25–0.35 nm; Br–Br: ≥0.37 nm) , confirming the balance between attractive hydrogen bonds and repulsive van der Waals forces that stabilize the 2D architecture.

Table 8. Binding energy ΔE_b of Br_4Py monolayer *M2* as a function of lattice constants *b* and *c* (2.120 – 2.240 nm) at a fixed interaxial angle β = 90°.

c / nm / b / nm	ΔE_b / eV						
	2.120	2.140	2.160	2.180	2.200	2.220	2.240
2.120	0.061	0.065	0.068	0.066	0.065	0.063	0.061
2.140	0.065	0.069	0.071	0.071	0.069	0.067	0.065
2.160	0.066	0.071	0.072	**0.073**	0.071	0.070	0.067
2.180	0.067	0.071	**0.073**	0.072	0.071	0.068	0.067
2.200	0.066	0.068	0.072	0.071	0.070	0.068	0.065
2.220	0.064	0.068	0.070	0.070	0.068	0.066	0.064
2.240	0.061	0.065	0.067	0.067	0.065	0.064	0.060

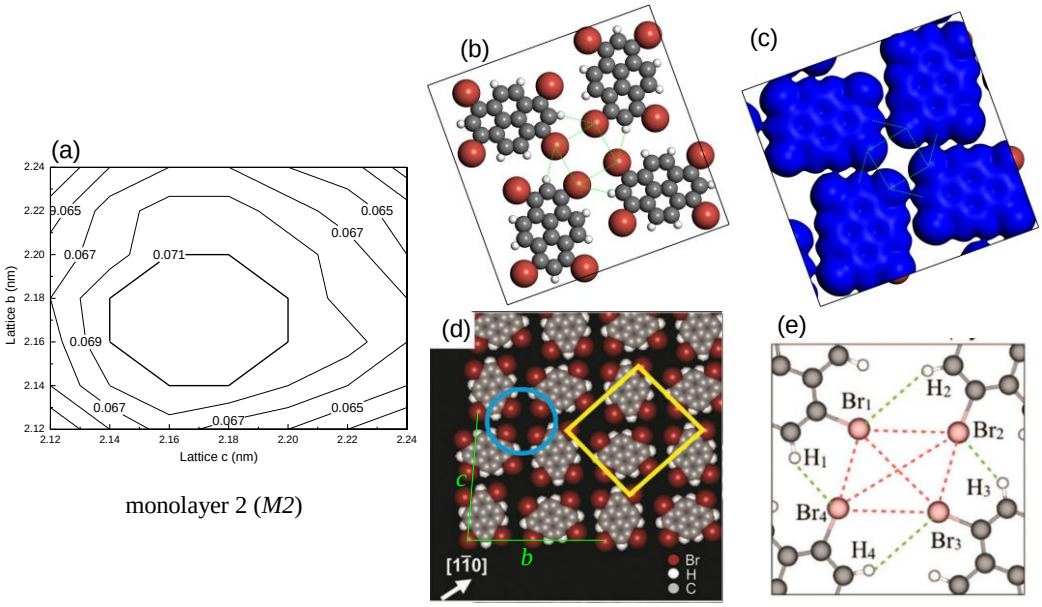

Fig. 4. (a) Contour plot of the ΔE_b landscape for Br_4Py monolayer 2 (*M2*) as a function of lattice constants *b* and *c* (2.120 – 2.240 nm) at a fixed interaxial angle β = 90°; (b, d) Atomic-resolution structure of *M2*, highlighting molecular packing symmetry and lattice parameters; (c) Electron density distribution mapped to intermolecular bonding sites, revealing charge redistribution at halogen/hydrogen bonds; (e) Intermolecular interaction motifs in *M2*, including Br–Br repulsion and Br–H attraction pathways. (d-e) are taken from the literature [10].

Conclusion

The structural evolution of Br4Py molecular assemblies was systematically investigated using CASTEP-based first-principles calculations with ultrasoft pseudopotentials. Total energy analysis across monomer, chain (*C1*-*C3*), and monolayer (*M1*-*M2*) configurations revealed thermodynamic stability ($\Delta E_b > 0$) governed by synergistic Br–H hydrogen bonding and Br–Br halogen interactions, consistent with established self-assembly paradigms for halogenated aromatic systems. Computational validation through direct comparison with STM-derived lattice parameters confirms the predictive accuracy of our model, with *M1* (ΔE_b = 0.072 eV) and M2 (ΔE_b = 0.073 eV) exhibiting nearly identical formation propensities. This energetic equivalence suggests competing assembly pathways dictated by distinct structural hierarchies: *M1* arises from cooperative packing of complementary chains *C1* and *C2*, optimized through dominant Br–H interactions ($D_{Br\text{-}H}$ = 0.323 nm), while *M2* emerges from homologous *C3* chain assembly mitigating Br–Br repulsion through extended separation ($D_{Br\text{-}Br} \geq$ 0.400 nm). Crucially, the metal substrate (Au(111))

introduces epitaxial constraints that modulate lattice parameters (*a, b, β*) via substrate-mediated strain effects, as evidenced by 5-6% deviations in experimental versus theoretical dimensions. This substrate-adsorbate coupling highlights the necessity of integrating interfacial charge transfer and geometric confinement in predictive models of surface-supported molecular architectures.

Funding

This work was supported by the National Natural Science Foundation of China (Grant No. 62374148), Central Leading Local Science and Technology Development Special Project (Grant No.YDZJSX20231A031).

Author Contributions

Ye Jingrong: Writing – original draft. Wu Taiquan: Writing – review & editing; Visualization; Validation; Methodology; Investigation; Data curation. Yu Binkai: Writing – original draft. Yan Shubin: Conceptualization; Supervision; Formal analysis.

Data Availability Statement

No data was used for the research described in the article.

References

[1] Whitesides, G. M.; Mathias, J. P.; Seto, C. T. *Science* **1991**, 254, 1312-1319. doi:10.1126/science.1962191

[2] Bubnov, A.; Cigl, M.; Sedláková, N.; Pociecha, D.; Böhmová, Z.; Hamplová, V. *Liq. Cryst.* **2020**, 47, 2276-2291. doi:10.1080/02678292.2020.1783586

[3] He, Y.; Tang, Y.; Zhang, Y.; MacFarlane, L.; Shang, J.; Shi, H.; Xie, Q.; Zhao, H.; Manners, L.; Guo, J. *Appl. Phys. Rev.* **2022**, 9, 021301. doi:10.1063/5.0083099

[4] Hadjivasiliou, Z.; Kruse, K. *Phys. Rev. Lett.* **2023**, 131, 208402.1-208402.6. doi:10.1103/PhysRevLett.131.208402

[5] Ulman, A. *Chem. Rev.* **1996**, 96, 1533-1554. doi:10.1021/cr9502357

[6] René, S.; Vermette, J.; Hassen, W. M.; Dubowshi, J. J. *Appl. Phys. Lett.* **2021**, 118, 222102.1-222102.6. doi:10.1063/5.0055031

[7] Pochan, D.; Scherman, O. *Chem. Rev.* **2021**, 121, 13699-13700. doi:10.1021/acs.chemrev.1c00884

[8] Li, J.; Zhang, Y.; Shi, Y.; Deng, K.; Zeng, Q. *Nano Res.* **2025**, 18, 455-463. doi:10.26599/NR.2025.94907099
[9] Auffinger, P.; Hays, F. A.; Westhof, E.; Ho, P. S. *P. Natl. Acad. Sci. USA* **2004**, 101, 16789-16794. doi:10.1073/pnas.0407607101
[10] Yang, Q.; Wu, Q.; Zhang, X.; Yang, X.; Li Q. *Mol. Phys.* **2022**, 120, 14-22. doi:10.1080/00268976.2022.2102548
[11] Yu, K.; Liu, Y.; Fu, B.; Zhang, R. W.; Ma, D. S.; Li, X. P.; Yu, Z. M.; Liu, C. C.; Yao, Y. *Phys. Rev. B* **2024**, 109, 125423-125429. doi:10.1103/PhysRevB.109.125423
[12] Cappelletti, D.; Falcinelli, S.; Pirani, F. *Phys. Chem. Chem. Phys.* **2024**, 26, 7971-7987. doi:10.1039/D3CP05871A
[13] Lee, D. C.; Cao, B.; Jang, K.; Forster, P. M. *J. Mater. Chem.* **2010**, 20, 867-873. doi:10.1039/b917601b
[14] Pham, T. A.; Song, F.; Nguyen, M. T.; St**ö**hr, M. *Chem. Commun.* **2014**, **50**, 14089-14092. doi:10.1039/c4cc02753a
[15] Clair, S.; De Oteyza, D. G. *Chem. Rev.* **2019**, 119, 4717-4776. doi:10.1021/acs.chemrev.8b00601
[16] Badorreck, H.; Steinecke, M.; Jensen, L.; Ristau, D.; Jupé, M.; Müller, J.; Tonneau, R.; Moskovkin, P.; Lucas, S.; Pflug, A.; Grinevičiūtė, L.; Selskis, A.; Tolenis, T. *Opt. Express* **2019**, 27, 22209-22225. doi:10.1364/OE.27.022209
[17] Wu, T. Q.; Shen, L. F.; Huang, B. Y.; Liu, G.; Zhang, W.; Cui, Y.; Chen, C.; Wang, X. Y.; Yan, S. B. *Phys. Lett. A* **2024**, 518, 129702.1-129702.8. doi:10.1016/j.physleta.2024.129702
[18] Ma, L.; Lu, Y.; Chen, Y.; Lu, T.; Yuan, G. *Mater. Res. Express* **2022**, 9, 025305.1-025305.12 doi:10.1088/2053-1591/ac4f87
[19] Perdew, J. P.; Burke, K.; Ernzerhof, M. *Phys. Rev. Lett.* **1996**, 78, 3865-3868. doi:10.1103/PHYSREVLETT.77.3865
[20] Wei, J.; Xia, Z.; Xia, Y.; He, J. *Phys. Rev. B*, **2024**, 110, 1-13. doi:10.1103/PhysRevB.110.035205
[21] Boran, Y.; Kara, H. *Braz. J. Phys.* **2024**, 54, 159.1-159.9. doi:10.1007/s13538-024-01523-w.
[22] Qin, H.; Zheng, Q.; Zhou, Y. X.; Li, F.; Li, H. D.; Liu, Q. J.; Liu, Z. T. *J. Mol. Model.* **2024**, 30, 7-15. doi:10.1007/s00894-023-05800-4
[23] Florence, A. J.; Bardin, J.; Johnston, B.; Shankland, N.; Griffin, T. A. N.; Shankland, K. *Z. Kristallogr. Suppl.* **2009**, 2009, 215-220. doi:10.1524/zksu.2009.0031
[24] Guo, Z. H.; Yan, X. H.; Xiao, Y. *Phys. Lett. A* **2010**, 374, 1534-1538. doi:10.1016/j.physleta.2010.01.060
[25] Segall, M. D.; Lindan, P. J. D.; Probert, M. J.; Pickard, C. J.; Hasnip, P. J.; Clark, S. J.; Payne, M. C. *J. Phys.: Condens. Matter* **2002**, 14, 2717-2744. doi:10.1088/0953-8984/14/11/301
[26] Nieckarz, K.; Szabelski, P.; Nieckarz, D. *Surf. Sci.* **2022**, 719,

122041.1-122041.13. doi:10.1016/j.susc.2022.122041
[27] Tuan, A. P.; Song, F.; Nguyen, M. T.; Zenshen, L.; Florian, S.; Meike, S. *Chem. Eur. J.* **2016**, 22, 5937-5944. doi:10.1002/chem.201601012